An Hα/X-ray orphan cloud as a signpost of intracluster medium clumping

Chong Ge [ORCID],[1]★ Rongxin Luo [ORCID],[1] Ming Sun [ORCID],[1]★ Masafumi Yagi,[2] Pavel Jáchym,[3] Alessandro Boselli,[4] Matteo Fossati [ORCID],[5] Paul E. J. Nulsen,[6] Craig Sarazin,[7] Tim Edge,[1] Giuseppe Gavazzi,[5] Massimo Gaspari [ORCID],[8,9] Jin Koda,[10] Yutaka Komiyama[2] and Michitoshi Yoshida [ORCID][11]

[1]*Department of Physics and Astronomy, University of Alabama in Huntsville, Huntsville, AL 35899, USA*
[2]*Optical and Infrared Astronomy Division, National Astronomical Observatory of Japan, 2-21-1, Osawa, Mitaka, Tokyo 181-8588, Japan*
[3]*Astronomical Institute, Academy of Sciences of the Czech Republic, Bočnĺ II 1401, 14100 Prague, Czech Republic*
[4]*Aix Marseille Université, CNRS, LAM (Laboratoire d' Astro physique de Marseille) UMR 7326, F-13388 Marseille, France*
[5]*Dipartimento di Fisica G. Occhialini, Universitá degli Studi di Milano Bicocca, Piazza della Scienza 3, I-20126 Milano, Italy*
[6]*Center for Astrophysics | Harvard & Smithsonian, Cambridge, MA 02138, USA*
[7]*Department of Astronomy, University of Virginia, P.O. Box 400325, Charlottesville, VA 22901-4325, USA*
[8]*INAF, Osservatorio di Astrofisica e Scienza dello Spazio, via P. Gobetti 93/3, I-40129 Bologna, Italy*
[9]*Department of Astrophysical Sciences, Princeton University, 4 Ivy Lane, Princeton, NJ 08544, USA*
[10]*Department of Physics and Astronomy, Stony Brook University, 100 Nicolls Rd., Stony Brook, NY 11794-3800, USA*
[11]*Subaru Telescope, National Astronomical Observatory of Japan, 650 North A'ohoku Place, Hilo, HI 96720, USA*

ABSTRACT

Recent studies have highlighted the potential significance of intracluster medium (ICM) clumping and its important implications for cluster cosmology and baryon physics. Many of the ICM clumps can originate from infalling galaxies, as stripped interstellar medium (ISM) mixing into the hot ICM. However, a direct connection between ICM clumping and stripped ISM has not been unambiguously established before. Here, we present the discovery of the first and still the only known isolated cloud (or orphan cloud [OC]) detected in both X-rays and Hα in the nearby cluster A1367. With an effective radius of 30 kpc, this cloud has an average X-ray temperature of 1.6 keV, a bolometric X-ray luminosity of $\sim 3.1 \times 10^{41}$ erg s^{-1}, and a hot gas mass of $\sim 10^{10}$ M$_{\odot}$. From the Multi-Unit Spectroscopic Explorer (*MUSE*) data, the OC shows an interesting velocity gradient nearly along the east-west direction with a low level of velocity dispersion of ~ 80 km s^{-1}, which may suggest a low level of the ICM turbulence. The emission line diagnostics suggest little star formation in the main Hα cloud and a low-ionization (nuclear) emission-line regions like spectrum, but the excitation mechanisms remain unclear. This example shows that stripped ISM, even long after the initial removal from the galaxy, can still induce ICM inhomogeneities. We suggest that the magnetic field can stabilize the OC by suppressing hydrodynamic instabilities and thermal conduction. This example also suggests that at least some ICM clumps are multiphase in nature and implies that the ICM clumps can also be traced in Hα. Thus, future deep and wide-field Hα surveys can be used to probe the ICM clumping and turbulence.

Key words: galaxies: clusters: individual: Abell 1367 – galaxies: clusters: intracluster medium – galaxies: ISM – X-rays: galaxies: clusters.

1 INTRODUCTION

Galaxy clusters grow hierarchically through merging and the accretion of smaller structures along the cosmic filaments, which are continuously channeling dark matter, galaxies, and gas into clusters. As galaxies enter the cluster environment filled with hot intracluster medium (ICM) with $T \sim 10^7 - 10^8$ K, their interstellar medium (ISM) is depleted by ram pressure and turbulent/viscous stripping from ICM (e.g. Gunn & Gott 1972; Quilis, Moore & Bower 2000). These stripping processes are very important to the evolution of the cluster galaxies through rapidly quenching their star formation (SF) activities, and eventually may turn blue disc galaxies into red galaxies

(e.g. Boselli & Gavazzi 2006). The stripping tails of cluster late-type galaxies have been observed from radio, mm, IR, and optical to X-ray (e.g. Gavazzi et al. 2001; Yoshida et al. 2002; Chung et al. 2007; Yagi et al. 2007; Kenney et al. 2008; Sivanandam, Rieke & Rieke 2010; Sun et al. 2010; Merluzzi et al. 2013; Jáchym et al. 2014; Boselli et al. 2016; Chen et al. 2020). In contrast to the early general wisdom that the stripped cold gas will simply mix with the hot ICM and be heated, now it is known that some fraction of the stripped ISM can collapse and form stars in the galactic halo and the intracluster space, especially in high-ICM-pressure environments (e.g. Sun, Donahue & Voit 2007b; Yoshida et al. 2008; Smith et al. 2010; Yagi et al. 2013; Poggianti et al. 2016).

Apart from the stripped tails close to their host galaxies, recent H I surveys have also revealed the existence of a population of optically dark, isolated H I clouds in galaxy clusters (e.g. Davies

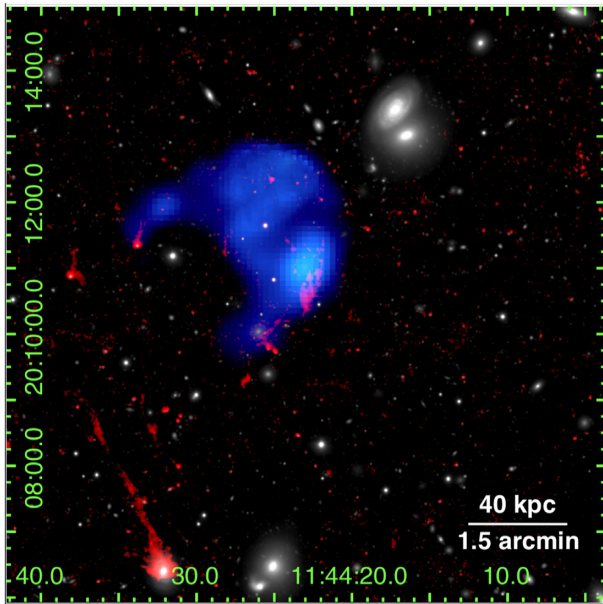★ E-mail: chong.ge@uah.edu (CG); ming.sun@uah.edu (MS)

Figure 1. Three-colour composite X-ray/optical image around the OC. White: *Subaru r*-band image; red: *Subaru* net Hα image; blue: *XMM* 0.5–2 keV image. The RA and Dec. are in J2000.

et al. 2004; Kent et al. 2007). The typical cloud mass is ~10^7 $M_\odot$ with a size around a few kpc (e.g. Taylor et al. 2012; Burkhart & Loeb 2016). Despite the initial excitement for the so-called 'dark galaxies', follow-up studies (e.g. Duc & Bournaud 2008; Taylor et al. 2016) suggest that these isolated clouds are most likely debris of ram pressure stripping (RPS) and tidal interaction.

Around the same time, ICM clumping has been revealed in the X-ray data (e.g. Nagai & Lau 2011; Simionescu et al. 2011; Churazov et al. 2012; Eckert et al. 2015; Morandi et al. 2017). Many of the X-ray clumps are likely evaporating cold gas removed from galaxies (e.g. Dolag et al. 2009; Vazza et al. 2013). The stripped gas clouds induce inhomogeneity or clumpiness in the ICM. Since the X-ray emissivity of the ICM scales with the square of gas density, ICM clumpiness can bias the measured gas density, which will further bias the gas mass, entropy, pressure, and cluster mass (e.g. Nagai & Lau 2011; Simionescu et al. 2011; Vazza et al. 2013). In addition to clumpiness, turbulence in the ICM provides additional pressure against gravity, thus it can also bias the mass determinations assuming hydrostatic equilibrium if it is not accounted for (e.g. Lau, Kravtsov & Nagai 2009). The characterization of ICM clumpiness and turbulence is important for current and next-generation surveys in the X-ray and millimetre via the Sunyaev–Zel'dovich effect, as well as using clusters as precise cosmological probes. However, there is limited information about the properties of individual ICM clumps from both observations and simulations.

We recently discovered an isolated X-ray clump with a counterpart in the form of warm ionized gas in the nearby galaxy cluster A1367, which is a dynamically unrelaxed cluster in the Coma supercluster (e.g. Sun & Murray 2002; Cortese et al. 2004). This cloud was first discovered in a narrow-band Hα imaging survey of A1367 (Yagi et al. 2017). However, its velocity was unknown so its origin remained unclear. It was classified as an orphan cloud (OC; Fig. 1). Our follow-up *XMM* observation in this field to study cluster merger shock and X-ray tails (Ge et al. 2019b) unexpectedly revealed a diffuse soft X-ray clump around the same position as the Hα OC (Fig. 1). Finally,

our new Multi-Unit Spectroscopic Explorer (*MUSE*) data confirm its association with A1367. The A1367 OC presents a great laboratory to study the evolution of the stripped ISM far away from the parent galaxy, and meanwhile to study the ICM clumping in detail. Here, we present a multiwavelength study for this isolated (or galaxy-less) cloud. We assume a cosmology with $H_0 = 70$ km s^{-1} Mpc^{-1}, $\Omega_m = 0.3$, and $\Omega_\Lambda = 0.7$. At A1367's redshift of $z = 0.022$, 1 arcsec = 0.445 kpc.

2 DATA ANALYSIS

2.1 *XMM-Newton* data processing

We analysed the data with the Obsid of 0823200101 (PI: M. Sun; total time: 71.6 ks; clean time: 66.8 ks for MOS and 50.4 ks for pn) for the properties of OC. The mosaic image of A1367 is from our previous study (Ge et al. 2019b), updated with a new observation with Obsid of 0864410101 (PI: C. Ge; total time: 40.0 ks; clean time: 32.8 ks for MOS and 18.2 ks for pn). We processed the *XMM* data using the EXTENDED SOURCE ANALYSIS SOFTWARE (ESAS), as integrated into the *XMM* SCIENCE ANALYSIS SYSTEM (SAS; version 17.0.0), following the procedures in Ge et al. (2019a). We reduced the raw event files from MOS and pn CCDs using tasks emchain and epchain, respectively. The solar soft proton flares were filtered out with mos-filter and pn-filter. The point sources were detected by task cheese and then visually inspected and properly excluded. We used mos-spectra and pn-spectra to produce event images and exposure maps, as well as to extract spectra and response files. The instrumental background images and spectra were modelled with mos_back and pn_back. We combined the event images, background images, and exposure maps from MOS and pn with comb. We used adapt to produce the final background subtracted, exposure corrected, and smoothed image (Fig. 2). The spectra from MOS/pn were fitted jointly with the XSPEC package. The nearby local background was used for fitting spectra. We used the ATOMDB (version 3.0.8) database of atomic data and the solar abundance table from Asplund et al. (2009). The Galactic column density $N_H = 1.91 \times 10^{20}$ cm^{-2} was from the NHtot tool (Willingale et al. 2013).

2.2 *MUSE* data processing

The OC was observed with the *MUSE* (Bacon et al. 2010) on the *Unit Telescope 4* (*Yepun*) of the *Very Large Telescope* (*VLT*) during the nights of 2020 February 25 and 2020 March 17, under the European Southern Observatory (ESO) program 0104.A-0268(A) (PI: M. Sun). Both nights were clear for photometry with seeing of 0.″71–1.″38 (a median value of 0.″88). Adopting the wide-field mode, four exposures (820 s each), in two slightly dithered positions, were taken for a total time of 0.91 h. The wavelength coverage is 4750–9350 Å with a spectral resolution of ~2600 at the wavelength of the OC's Hα line. We also carried out a sky background observation for 2 min at ~150 arcsec from the OC.

The raw data of each pointing were reduced using the *MUSE* pipeline (version 2.8.1; Weilbacher et al. 2012, 2020) with the ESO Recipe Execution Tool (EsoRex; ESO CPL Development Team 2015), which performed the standard steps to calibrate the individual exposures and combine them into a datacube. We also used the ZURICH ATMOSPHERE PURGE SOFTWARE (ZAP; Soto et al. 2016) to improve the sky subtraction. The CubeMosaic class implemented in the MUSE PYTHON DATA ANALYSIS FRAMEWORK (MPDAF) package (Bacon et al. 2016) was used to combine the individual datacube of
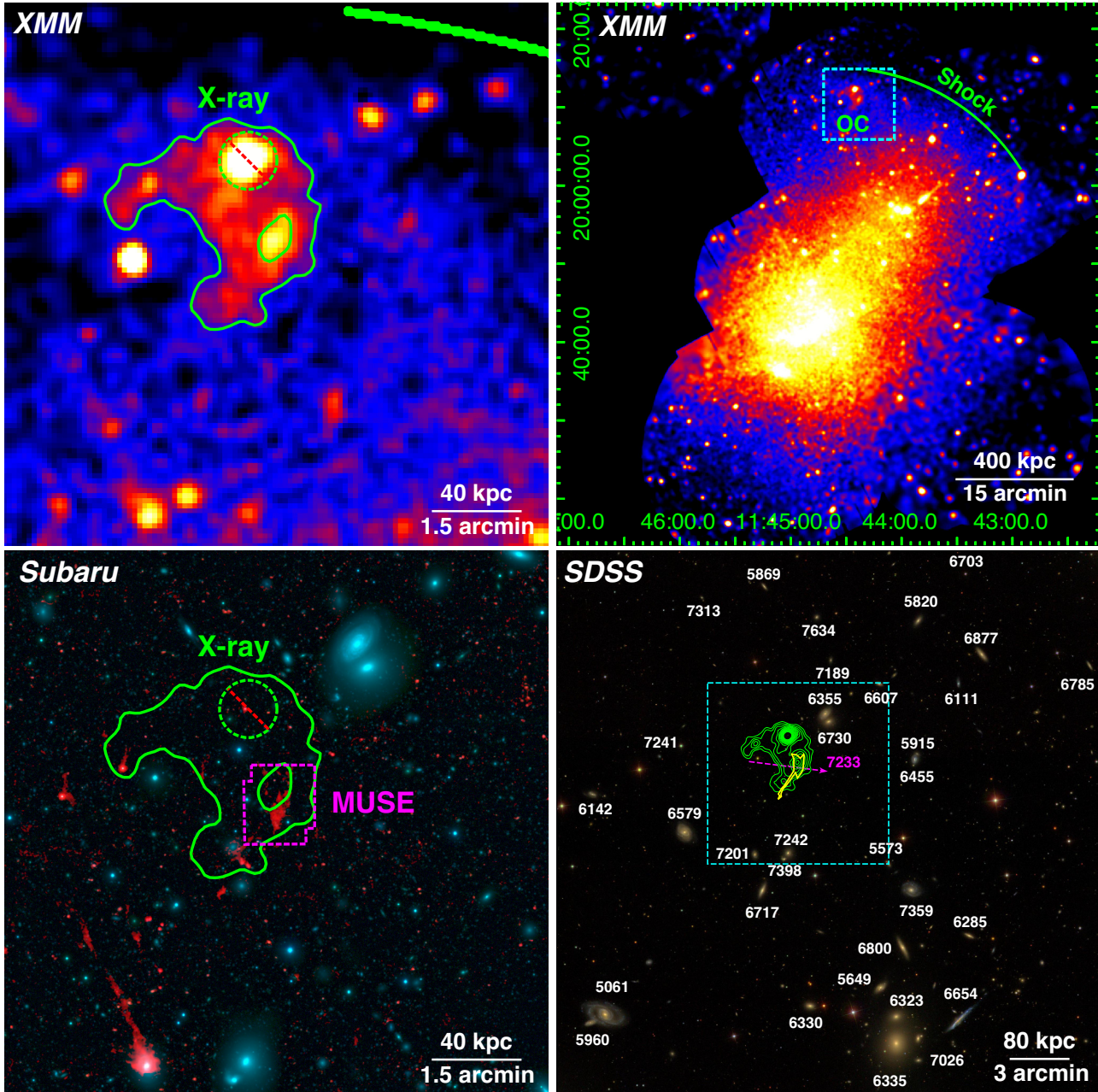
Figure 2. X-ray and optical images of the OC and nearby galaxies. Upper left: the 0.5–2 keV *XMM* image of the OC, background subtracted and exposure corrected. The green contour outlines its X-ray morphology and the dashed circle marks a bright point source that is most likely an unrelated background AGN. Upper right: the 0.5–2 keV *XMM* mosaic of A1367 (background subtracted and exposure corrected), with the dashed cyan box showing the field of the left-hand panels. The OC is marked and the green arc marks a merger shock front (Ge et al. 2019b). Part of the green arc is shown in the upper left panel. Lower left: the *Subaru* three-colour composite image (red: net Hα; green: *r*-band; blue: *g*-band) of the same field as the upper left panel. The dashed magenta region shows the *MUSE* FOV. Lower right: *SDSS* image around the OC, with the green contours from X-rays. The yellow contour highlights the Hα cloud from the *Subaru* image (Yagi et al. 2017). The velocities of galaxies in A1367 are marked with white numbers (in a unit of km s^{-1}). The velocity of the OC is marked with a magenta number. The direction of the velocity gradient is marked with a dashed magenta arrow (see Fig. 3 below). The dashed cyan box shows the field of the left-hand panels.

each pointing into a final datacubes mosaic. Astrometry is calibrated with bright *2MASS* stars in the field.

We used the public IDL software KUBEVIZ (Fossati et al. 2016) to perform the spectral analysis for the final datacube mosaic. We first corrected the Galactic extinction by using the colour excess from the recalibration (Schlafly & Finkbeiner 2011) of the dust map of

Schlegel, Finkbeiner & Davis (1998), adopting a Galaxy extinction law from Fitzpatrick (1999) with $R_V = 3.1$. Given the seeing value and the faintness of the diffuse emission, we also smoothed the datacube with a Gaussian kernel of 6 pixels (or 1.″2). We fitted the Hβ, [O III], [O I], [N II], Hα, and [S II] emission lines with Gaussian profiles to obtain the emission-line fluxes, the velocity, and the velocity
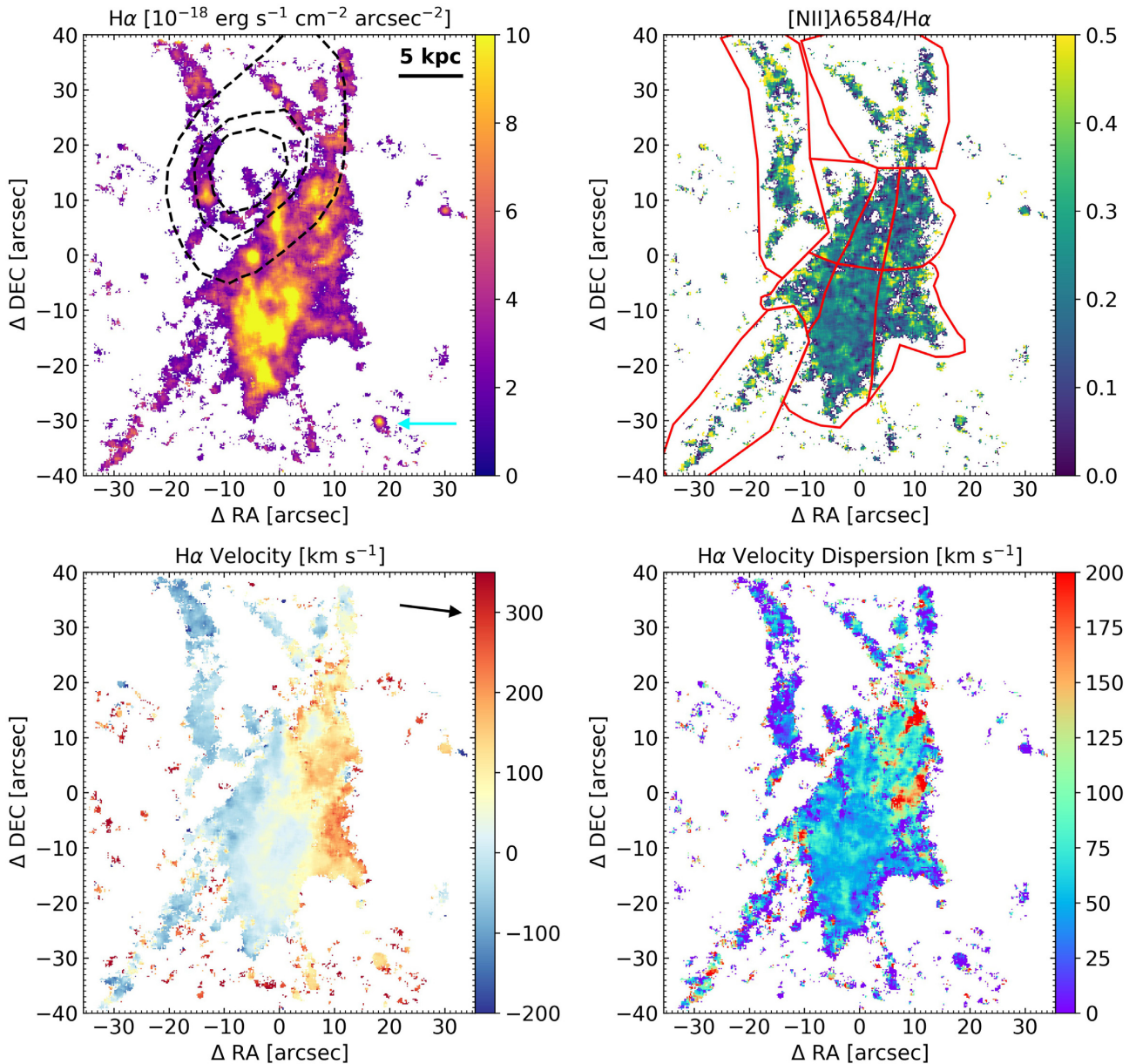
Figure 3. The 2D maps on the properties of the warm, ionized gas in the OC from the *MUSE* observations, relative to (11:44:22.74, +20:10:44.60). Upper left: H α surface brightness. The black contours in the dashed lines show the central X-ray emission of the OC, with the outer contour the same as the one around the X-ray peak in the left-hand panels of Fig. 2. The cyan arrow shows the only candidate H II region in the *MUSE* field. Upper right: [N II]/H α flux ratio. The red solid lines show the nine large regions where the total spectra are extracted for studies of line diagnostics and kinematics. Lower left: H α velocity (relative to $z = 0.024$). The black arrow shows the best-fitting direction of the velocity gradient. Lower right: H α velocity dispersion.

dispersion of the ionized gas. The 2D maps of H α surface brightness, [N II]/H α flux ratio, H α velocity, and velocity dispersion are shown in Fig. 3. We mask the spaxels with S/N < 5 or velocity error and velocity dispersion error > 50 km s^{-1}. We can also compare the total H α flux of the OC from the *MUSE* data with the result from Yagi et al. (2017) based on the narrow-band imaging data. We derive a total H α flux of $(4.6 \pm 0.1) \times 10^{-15}$ erg s^{-1} cm^{-2} from the full *MUSE* field. With the updated velocity and the [N II]/H α flux ratio, we revise the total H α flux of Yagi et al. (2017) to $(4.1 \pm 0.2) \times 10^{-15}$ erg s^{-1} cm^{-2} for Orphan 1 and $(4.8 \pm 0.2) \times 10^{-16}$ erg s^{-1} cm^{-2} for Orphan 2. The *MUSE* field of view (FOV) covers the whole Orphan 1 and part of Orphan 2, and the *MUSE* data are slightly deeper than

the narrow-band imaging data, the *MUSE* H α flux is consistent with the H α flux from the *Subaru* narrow-band data.

2.3 *APO/DIS* data processing

We observed the OC with the Dual Imaging Spectrograph (*DIS*) on the Apache Point Observatory (*APO*) on 2020 January 30, 2021 January 16, and 2021 February 4 (PIs: C. Sarazin & M. Sun). The first two nights were not photometric and a 6 arcmin long slit with a width of 2 arcsec was used. The third night on 2021 February 4 was nearly photometric and a 6 arcmin long slit with a width of 5 arcsec was used. On 2020 January 30, we observed the main body of the OC

on two slit positions (70 and 60 min, respectively). These data are superseded by the later *MUSE* data but allow us to verify the velocity consistency, $7201 \pm 28\,\mathrm{km\,s^{-1}}$ from *DIS* versus $7222 \pm 35\,\mathrm{km\,s^{-1}}$ from *MUSE* (uncertainty mainly from the uncertain *DIS* slit position) for the first slit position with the stronger detection than that of the other position. On 2021 January 16 and February 4, we observed two slit positions to the southeast of the OC that is outside of the *MUSE* field, in 70 and 40 min, respectively. The results are presented in Section 3.2.1. The dome flats were used. All *DIS* velocities are calibrated with both the arc lamp spectra and night sky lines. The heliocentric correction was also made for all measured velocities.

2.4 *Subaru* data processing

In Fig. 2, we used g, r, and net $H\alpha$ images. The $H\alpha$-on data were obtained on 2017 May 27 with the N-A-L671 narrow-band filter of Suprime-Cam as an integration of thirty-four $\leq$5-min exposures with a total integration time of 165 min under a natural seeing size of $0.''7-0.''9$. The data were reduced as described in Yagi et al. (2017). We used astrometry.net (Lang et al. 2012) to obtain an astrometric solution. Broadband images were obtained with the Hyper Suprime-Cam (HSC) in r and g bands on 2016 March 10 and 2017 March 27. The number of exposures, total exposure time, and typical seeing size were 11, 28.5 min and $0.''7$ in r band respectively, and 23, 66.5 min and $1.''0$ in g band respectively. The data were reduced with HSCPipe HSCPIPE version 4.0.5 (Bosch et al. 2018). We took the median of all the exposures. The r band data were also used for off-band of $H\alpha$. The on and off images were aligned and resampled with respect to WCS using SWARP (Bertin et al. 2002). The off image was then scaled and subtracted from the on image to obtain the net $H\alpha$ image. The remaining artefacts and stellar halo residuals were manually masked.

3 RESULTS

In general, the OC is $\sim$800 kpc in projection from the centre of A1367 with $r_{500} \approx 900$ kpc derived from an average $T_X = 3.5$ keV (Sun & Murray 2002) and $r_{500} - T_X$ relation (Sun et al. 2009). It is not far from the major axis of the cluster (NW $-$ SE). It is also located near a cluster merger shock front (Ge et al. 2019b). If it is truly located in the post-shock region, shock compression could have enhanced the density and X-ray luminosity of the OC, aiding to its discovery. In X-rays, the OC peaks around the main $H\alpha$ OC, but with an offset of $\sim$12 kpc. As shown in Fig. 3, there seems to be an anti-correlation between the X-ray peak and the $H\alpha$ emission, with the X-ray peak surrounded by $H\alpha$ filaments. There is an extension to the north but the analysis there is complicated by a bright background active galactic nucleus (AGN; more detail in Section 3.1.2). There is also an X-ray extension to the SE, just like the $H\alpha$ OC. Our recent deep *Subaru* $H\alpha$ image of the field reveals more $H\alpha$ emission scattered around the X-ray OC, suggesting that there is a complex of warm, ionized clouds around the main $H\alpha$ OC discussed in Yagi et al. (2017). The positional coincidence of the $H\alpha$ clumps and the X-ray OC justifies their association. As discussed in Section 4.1, the X-ray OC also cannot be a background cluster. The properties of the OC are summarized in Table 1.

3.1 X-ray properties of OC

The X-ray OC is asymmetric around its X-ray peak. Its umbrella-like morphology resembles the shape of a simulated isolated cloud moving in the ICM (e.g. Calura, Bellazzini & D'Ercole 2020). A

Table 1. Properties of the OC.

RA	$11^\mathrm{h}44^\mathrm{m}23^\mathrm{s}.2$
Dec.	$+20^\circ 11' 00''.2$
z	0.0241
radius (kpc)	30
SFR ($\mathrm{M_\odot\,yr^{-1}}$)	$< 10^{-3}$
kT_X (keV)	1.6 ± 0.1
X-ray Abundance ($\mathrm{Z_\odot}$)	0.14 ± 0.03
$L_{0.5-2\,\mathrm{keV}}$ ($10^{41}\,\mathrm{ergs\,s^{-1}}$)	1.3
L_{bol} ($10^{41}\,\mathrm{ergs\,s^{-1}}$)	3.1
n_e ($10^{-3}\,f_X^{-1/2}\,\mathrm{cm^{-3}}$)[a]	3.1
M_X ($10^{10}\,\mathrm{M_\odot}$)	$1.0(f_X/1.0)^{1/2}$
$M_{H\alpha}$ ($10^7\,\mathrm{M_\odot}$)[b]	$8.0(f_{H\alpha}/0.01)^{1/2}$

Notes. [a]The average electron density of the X-ray gas. f_X and $f_{H\alpha}$ are the filling factor of the X-ray and $H\alpha$ gas respectively. [b]For the $H\alpha$ mass, the Case B recombination is assumed and we approximate the $H\alpha$ OC main body as a sphere with a radius of 8 kpc. Despite all the uncertainties, the mass of the warm gas is expected to be much smaller than that of the hot gas.
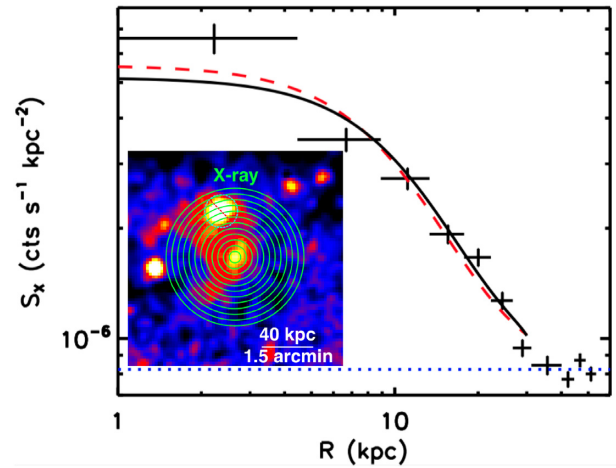

Figure 4. The SBP of the OC. The solid black line is the best fit of a β-model convolved with the *XMM* PSF, while the dashed red line is the β-model without correction for the PSF. The dotted blue line is the local background level. The inset in the left corner shows the annuli for the SBP extraction. The annuli are centred on the X-ray peak.

radial surface brightness profile (SBP) centred on its peak shows an effective radius of $\sim$30 kpc (Fig. 4). It has a lower temperature than that of the surrounding ICM (1.6 versus 2.9 keV) from *XMM* data. The best-fitting abundance from the single-T model is only $\sim$0.14 solar but that is biased low due to the intrinsically multi-T gas in the OC. The total X-ray bolometric luminosity is $3.1 \times 10^{41}\,\mathrm{ergs\,s^{-1}}$, comparable to those of massive cluster galaxies (e.g. Sun et al. 2007a). The cooling time of the X-ray gas in the OC is more than 3.6 Gyr so the warm gas is not the product of cooling in the soft X-ray gas. Instead, the X-ray OC likely glows because of the mixing between the cold gas and the surrounding hot ICM. More details are presented below.

3.1.1 Spectral Properties of the X-ray OC

We extracted the spectra of the OC from the *XMM* data, excluding the bright point source near the northern edge of the OC. We also extracted the spectra of the immediate surroundings as the

Table 2. X-ray spectral models for the OC.

Model	Parameters	C-stat/degrees of freedom
APEC	$kT = 1.6 \pm 0.1$, $Z = 0.14 \pm 0.03$, $L_T = 1.3 \pm 0.1$	269/219
APEC+PL	$kT = 1.1 \pm 0.1$, $Z = 0.21 \pm 0.03$, $L_T = 7.4 \pm 0.4$, $\Gamma = (1.7)$, $L_P = 1.5 \pm 0.1$	231/216
APEC+APEC	$kT_1 = 1.0 \pm 0.1$, $Z_1 = (0.3)$, $kT_2 = 3.6 \pm 0.7$, $Z_2 = (0.3)$, $N_1/N_2 = 0.36$	244.7/216
APEC+APEC	$kT_1 = 0.97 \pm 0.04$, $Z_1 = (1.0)$, $kT_2 = 2.7 \pm 0.3$, $Z_2 = (0.3)$, $N_1/N_2 = 0.1$	250.6/216
CEMEKL	$\alpha = 1.5 \pm 0.2$, $kT_{max} = (2.9)$, $Z = (0.3)$, $L_T = 1.3 \pm 0.1$	240.3/220

Note. The Galactic absorption (1.91×10^{20} cm^{-2}) is included in all cases with a model of TBABS. L_T (0.5–2 keV) and L_P (2–10 keV) are the luminosity of APEC/CEMEKL and power-law model with unit of 10^{41} erg s^{-1}. The unit for kT is keV and the unit for the abundance Z is solar. Parameters in parentheses are fixed. CEMEKL is a multitemperature plasma emission model with emission measures following a power-law distribution in temperature: EM(T)$\propto (T/T_{max})^\alpha$.

local background. We emphasize that the mixing between stripped cold ISM and hot ICM can produce the multiphase gas as for the case of OC. However, physically motivated X-ray spectral models to study the mixing clouds are unavailable. Nevertheless, we can still gain insight with simple models. The spectra are fitted with different models in XSPEC, with results detailed in Table 2. The single-T model gives a very low abundance, which is most likely the result of intrinsically multi-T gas in the OC (e.g. Sun et al. 2010). Including an additional power-law model (for X-ray point sources unresolved by *XMM*) or using a two-T model results in better fits, because these models include more free parameters to provide a better approximation. We also tried a multitemperature model (CEMEKL), first used on stripped tails by Sun et al. (2010). The maximum temperature of CEMEKL is fixed to that of the surrounding ICM, and its abundance is fixed to the typical value of the ICM (0.3 solar). The better fitting statistic from the CEMEKL model also suggests a multi-T nature of the OC. However, all these models only provide over-simplified and phenomenological fits to the X-ray OC, given the limited angular resolution and the limited statistics of the *XMM* data. On the other hand, the best-fitting temperature from the one-T model can be taken as the spectroscopic or effective temperature of the X-ray OC, and can be compared with the temperature of other multiphase gas like the stripped tails. The X-ray luminosity from these models is robust as e.g. APEC and CEMEKL models give consistent X-ray luminosity.

3.1.2 Bright X-ray point source in the X-ray OC

From the *XMM* spectra, the bright X-ray point source near the northern edge of the OC is best fitted with a power-law model, with a photon index of $\Gamma = 1.9 \pm 0.1$ and a flux of $f_{2-10\,keV} = 5.9 \times 10^{-14}$ ergs cm^{-2} s^{-1}. Its faint optical counterpart (SDSS J114425.15+201219.6) was selected as an AGN candidate (Richards et al. 2015). The log$N$ − log$S$ relation (Mateos et al. 2008) predicts an X-ray source density of 20 deg^{-2} above the flux of this source. Indeed, this X-ray point source is the brightest one within a radius of 8 arcmin in the *XMM* FOV, which corresponds to 18 deg^{-2}. Thus, this source is most likely a background AGN unrelated to the OC.

3.1.3 Gas density and mass of the X-ray OC

We estimate the hot gas density of the OC from the XSPEC normalization, assuming a spherical cloud of uniform density. The

APEC normalization η is

$$\eta = \frac{10^{-14}}{4\pi [D_A(1+z)]^2} \int n_e n_H dV \qquad (1)$$

where $z = 0.022$ is the redshift of A1367, D_A is the angular size distance at $z = 0.022$, n_e and n_H are electron and proton densities. Because the X-ray shape of the OC is asymmetric, we use an effective radius of $R_{OC} \sim 30$ kpc enclosing most of its diffuse X-ray emission. Fig. 4 shows the radial SBP of the OC centred at its X-ray peak. The SBP also suggests that the diffuse X-ray emission extends to around 30 kpc. The resultant average density is $n_e = 3.1 \times 10^{-3} f^{-1/2}$ cm^{-3}, where f is the filling factor of the X-ray emitting gas. The gas mass of the OC is $M_{OC} = 1.0 \times 10^{10} f^{1/2}$ M$_\odot$ for uniform density. We also try a β-model (Cavaliere & Fusco-Femiano 1976) convolved with *XMM* point spread function (PSF) to fit the SBP of OC as in Fig. 4. The β-model gas distribution is given by $n_{gas}(r) = n_0[1 + (r/r_c)^2]^{-3\beta/2}$, which is an analytical model with the derived X-ray SBP also following a β-model in the form of $I_X(r) = I_0[1 + (r/r_c)^2]^{1/2-3\beta}$. We use the analytical formula equation (10) of Ge et al. (2016) to convert the central surface brightness I_0 (from the β-model fitting to the SBP) to the central gas density n_0. The related central electron density is $4.6 \times 10^{-3} f^{-1/2}$ cm^{-3}. The gas cooling time t_{cool} at $n_e = 4.6 \times 10^{-3}$ cm^{-3} and $kT = 1.6$ keV and $Z = 0.5$ is $t_{cool} = 3.6$ Gyr. The gas cooling time at $n_e = 3.1 \times 10^{-3}$ cm^{-3} and $kT = 1.6$ keV and $Z = 0.14$ is $t_{cool} = 7.2$ Gyr.

3.2 Hα properties of OC

The Hα OC is composed of the main body covered by our *MUSE* observations, a SE trail, and some other clumps around the X-ray OC (Fig. 2). Our new *MUSE* observations not only confirm the association of the Hα OC with A1367, but also provide details on the kinematics and line diagnostics of the cloud, as shown in Fig. 3. There is a clear velocity gradient in the main body of the Hα OC and the velocity dispersion is typically small, ~80 km s^{-1}. Line diagnostics (see detail in Section 3.2.2) suggest little SF in the OC but the ionization mechanism remains unclear. Why is the brightest Hα emission offset from the brightest X-ray emission? OC is likely in a late evolutionary stage of mixing between the stripped cold ISM and the hot ICM as suggested below. The bright Hα clumps may be associated with the only surviving cold clouds while the bulk of the X-ray OC is free of cold gas now. Future H I and CO observations of the OC will be important to understand the evolution of the OC.
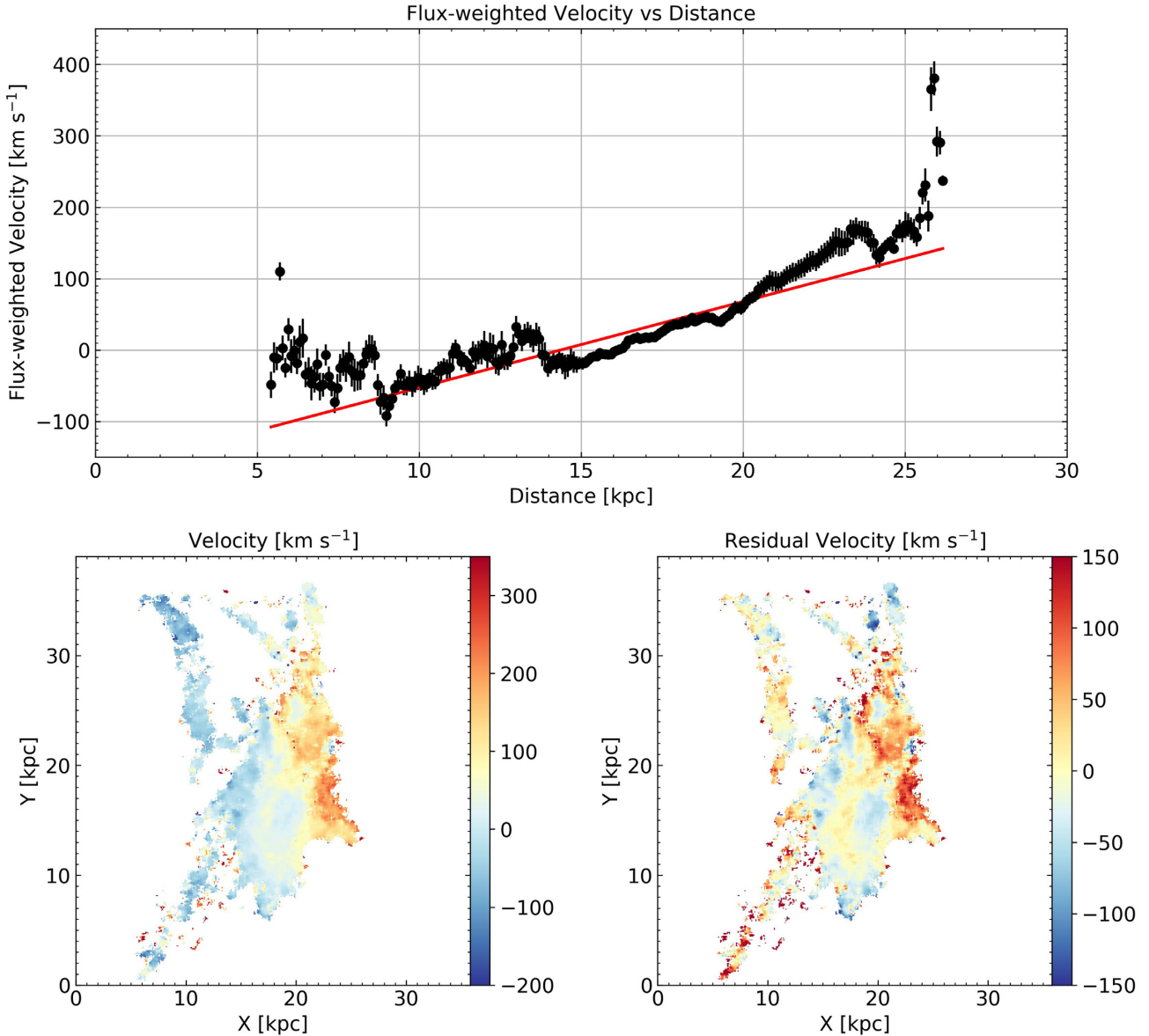
Figure 5. The best-fitting results of the velocity gradient for the ionized gas in the *MUSE* field. During the fitting process, we rotated the velocity map at a certain angle and calculated the flux-weighted average of the velocity in each column. The best-fitting direction of the velocity gradient is determined to have the lowest rms in the corresponding residual velocity map (velocity map – velocity gradient). Such an analysis determined the best-fitting direction of the velocity gradient, 7.1 deg clockwise from the west as shown in Fig. 3. The *MUSE* velocity map is then rotated accordingly to align the velocity gradient east–west here. Upper panel: the H α flux weighted velocity as a function of the distance from the eastern edge of the *MUSE* field, after the rotation. The black dots show the averaged velocities, weighted by the H α flux from spaxels in each column. The red solid line shows the best-fitting velocity gradient. Lower panels: the rotated velocity map and the corresponding residual map after removing the best-fitting velocity gradient.

3.2.1 Kinematics of the H α OC

From the integrated spectrum of the whole OC in the *MUSE* field, the redshift is measured to be 0.0241. The OC is likely moving westward as suggested by the umbrella-like X-ray morphology and the SE H α trail (Fig. 2; Yagi et al. 2017). The H α velocity map in Fig. 3 shows a nearly east–west velocity gradient. We estimate the velocity gradient by minimizing the velocity residuals relative to a model with a constant gradient from the *MUSE* velocity map. An angle of 7.1 $\pm$ 1.0 deg clockwise from the west, as shown in Fig. 3, results in the minimal velocity residual. The velocity gradient

along this direction is substantial, 12 km s^{-1} per kpc. The H α OC has a total velocity gradient of $\sim$200 km s^{-1} nearly aligned east–west (Figs 3 and 5). Such a large velocity gradient is higher than those typically found in isolated H I clouds (e.g. Cannon et al. 2015). We can also estimate the cloud's dynamical mass if we assume that the velocity gradient is due to rotation in a stripped disc. We extrapolate the velocity gradient (12 km s^{-1} per kpc) to the OC's radius of 30 kpc, then the dynamic mass is $M = v^2 r/G = 9.0 \times 10^{11}$ M$_\odot$. Thus, if the observed velocity gradient of the OC is the imprint of the rotation in the disc of its parent, its parent must be a massive galaxy. On the
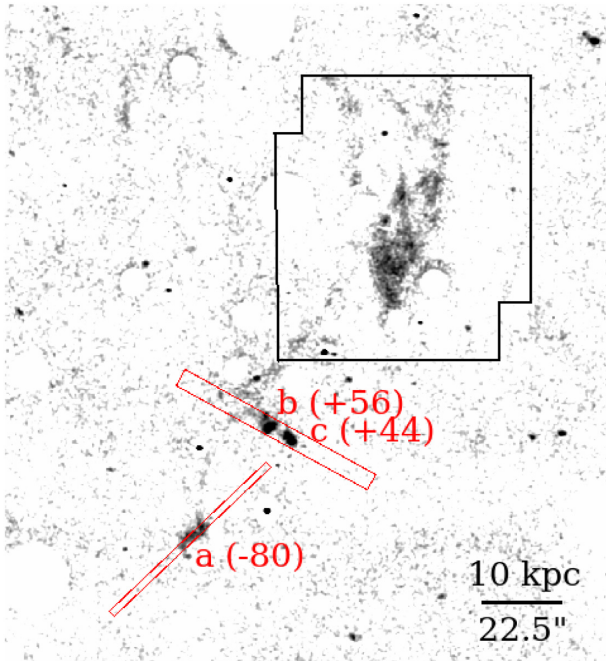
Figure 6. The *APO/DIS* slit positions at the southeast of the Hα OC. The velocities (in a unit of km s^{-1}, relative to $z = 0.024$ as in Fig. 3) are also shown. The image shows the net Hα emission from *Subaru*, with stars and galaxies masked out. The *MUSE* FOV is also shown in a black solid box.

other hand, the rotation pattern in the stripped ISM is not expected to be conserved for a long period of time after stripping (e.g. Boselli et al. 2021).

While the map of the velocity dispersion is shown in Fig. 3, we also spatially divided the *MUSE* FOV into nine large regions (see the upper right panel of Fig. 3) and examined the velocity dispersion there. The velocity dispersion in these regions ranges from 50 to 149 km s^{-1}, with a median value of ∼80 km s^{-1}. There are several positions to the west side of the OC with velocity dispersion as high as ∼180 km s^{-1} but the typical velocity dispersion is small. We can also derive the velocity dispersion of the cloud at ∼10 kpc scales from the velocity map shown in Fig. 3. The standard deviations of the velocity histogram, weighted or not weighted by the Hα flux, are 75 and 88 km s^{-1}, respectively. If the average velocity gradient of the OC is subtracted, those values decrease to 55 and 67 km s^{-1}, respectively. The above analysis examines the velocity dispersion of the warm gas at kpc − 10 kpc scales, indicating the small contribution from turbulence at those scales, at least in the warm gas.

We also obtained a few more velocities for the warm, ionized gas beyond the *MUSE* field from *APO/DIS*, as shown in Fig. 6. The three positions and the measured velocities are listed: a at (11:44:26.8 +20:09:16.3) − 7115 ± 37 km s^{-1}, b at (11:44:25.3 +20:09:46.3) − 7239 ± 29 km s^{-1}, c at (11:44:24.9 +20:09:43.1) − 7251 ± 26 km s^{-1}. Regions b and c are most likely H II regions from their high surface brightness (easily detected in 10 min with *DIS*), as also suggested by Yagi et al. (2017). [N II] and [S II] lines are also detected in regions b and c. We constrained [N II]/Hα ∼ 0.4 and [O I]/Hα < 0.2. As shown in Fig. 2, there are more Hα clumps around the OC. 2MASX J11443212+2006238 with an 85 kpc Hα is also nearby and has a similar velocity of 7214 km s^{-1} (Gavazzi et al. 2017; Yagi et al. 2017).

3.2.2 Line diagnostics of the Hα OC

We used emission-line diagnostics to examine the excitation mechanisms for the warm ionized gas in the OC. In order to enhance the S/N of faint emission lines, we again focus on those nine large regions shown in Fig. 3 and measure the Hβ, [O III], [O I], [N II], Hα, and [S II] emission-line fluxes from the co-added spectra within each region. The corresponding emission-line flux ratios are shown in Fig. 7. We used the criteria from Kewley et al. (2001) and Kauffmann et al. (2003) to classify the AGN, composite, and star-forming regions. The demarcation of Cid Fernandes et al. (2010) was used to separate the Seyfert and low-ionization (nuclear) emission-line regions (LI(N)ERs). As shown in Fig. 7, while the [N II]/Hα and [S II]/Hα flux ratios are low, the [O I]/Hα flux ratios are relatively high and the [O III]/Hβ flux ratios are also low, indicating the LI(N)ER-like emission of the ionized gas. This is a good example of LI(N)ER-like emission not in an active nucleus, but in an extragalactic region (also see Yoshida et al. 2012; Consolandi et al. 2017 for similar examples in stripped tails still close to the parent galaxy).

3.3 Hα – X-ray correlation for the OC

We also examined the diffuse Hα–X-ray correlation for the OC to compare with the tight correlation recently found for stripped tails still attached to their parent galaxies (Sun et al. 2021). Such a tight correlation supports the mixing of the stripped ISM with the hot ICM as the origin of the multiphase stripped tails. Five regions are selected (Fig. 8). Hα and X-ray surface brightnesses are measured in these regions, with emission from galaxies, background sources, and H II regions excluded. The bolometric X-ray flux in individual regions is from the spectral fitting with nearby local background (mostly from the ICM emission) subtracted. The Hα emission in regions 1–3 is robustly measured. There is some diffuse Hα emission in region 4, e.g. the diffuse tail, but H II regions (b and c in Fig. 6) and galaxies are removed. Some faint, diffuse Hα emission may also be present in region 5. However, the level of faint, diffuse Hα emission beyond the main body is quite uncertain, because of the uncertainty of the flat fielding at large scales and the subtraction of the light from other objects. Thus, only upper limits are estimated for regions 4 and 5. As shown in Fig. 8, away from the Hα OC, the X-ray-to-Hα ratio is elevated, as expected for a cloud that has long left its parent galaxy and evolved in the ICM for a long time. Most cold gas are already gone so active mixing may only proceed around the Hα OC. Is the high X-ray/Hα ratio related to the weak SF activity in the OC? Many stripped tails in the Sun et al. (2021) sample have very weak SF comparable to that in the OC (e.g. NGC 4569, ESO 137-002, CGCG 097-073, CGCG 097-079, and D100), but the X-ray/Hα ratios in their tails are all similar to the median value from Sun et al. (2021). Moreover, SF in the OC is outside of the main Hα OC but the X-ray/Hα ratio in the main Hα OC is the lowest among all regions of the OC. Thus, the weak SF in the OC should not account for its large X-ray-to-Hα ratio.

The mean temperature of the whole X-ray OC, 1.6 ± 0.1 keV, is higher than typical temperatures of X-ray tails of cluster late-type galaxies (∼0.9 keV, Sun et al. 2021), which may also suggest an advanced evolutionary stage of the X-ray OC as it mixes with the surrounding hotter ICM. We note that the elevation of X-ray emission and temperature of OC might be caused by the merger shock if the OC is truly in the post-shock region. The shock Mach number is M ∼ 1.6 (Ge et al. 2019b), which can produce a temperature jump of $T_J = 1.6$ (i.e. from 1.0 to 1.6 keV).
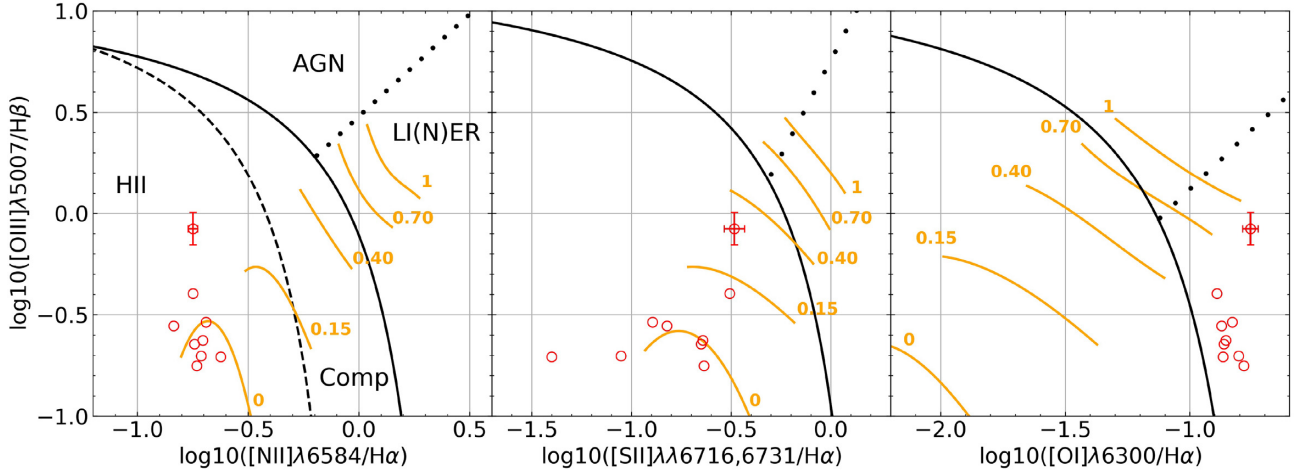
Figure 7. The emission line ratios in nine large spatial regions of the A1367 OC. The dashed, solid, and dotted lines show the criteria (from Kewley et al. 2001, Kauffmann et al. 2003 and Cid Fernandes et al. 2010) to separate the regions of SF, composite (Comp), AGN, and LI(N)ER, respectively. Typical errors in the ratios are plotted on the data points with the largest [O III]/Hβ ratio (from the region at ΔRA ~ 10 arcsec and ΔDec. ~ 8 arcsec in Fig. 3). The solid orange lines show the fractions (from 0 to 1) of Hα flux from radiative shocks as predicted by the models in Rich, Kewley & Dopita (2011). While the first two plots may suggest these regions as H II regions, the [O I]/Hα ratios in these regions are too high and there is no evidence of SF from the *GALEX* data.
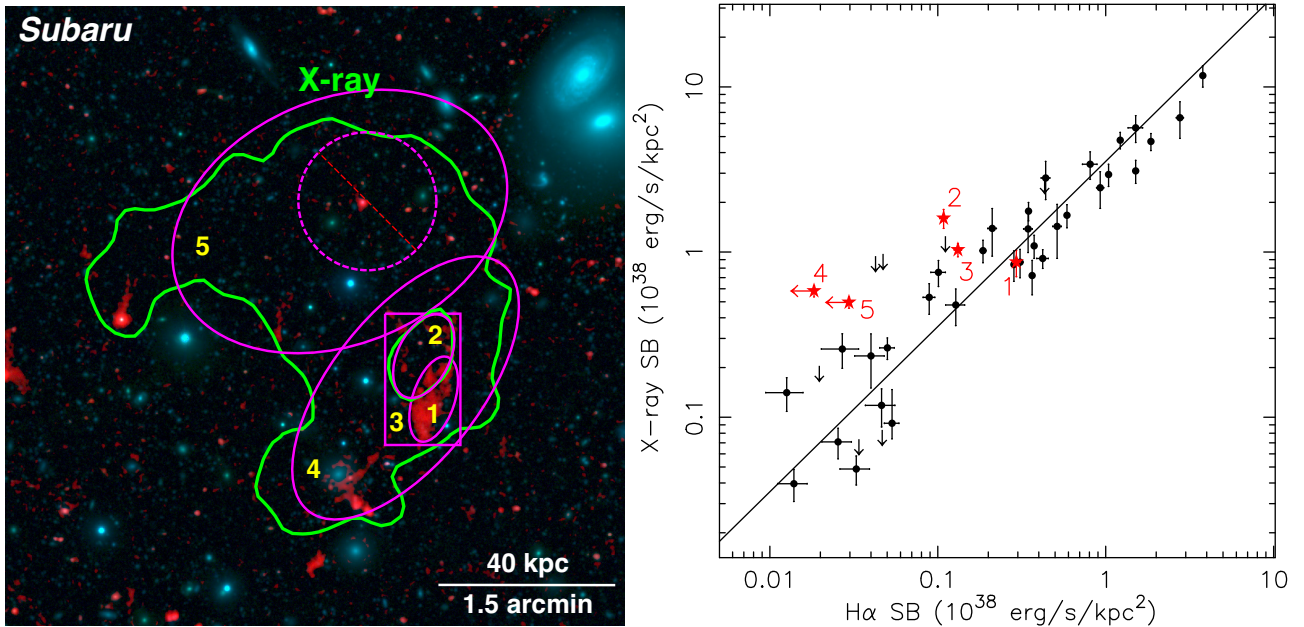

Figure 8. Left-hand panel: regions used to study the Hα–X-ray correlation. Regions 1 and 2 are ellipses around the Hα and X-ray peaks, respectively. Region 3 is a box excluding regions 1 and 2. Region 4 is an ellipse excluding region 3. Region 5 is an ellipse excluding the bright X-ray source and region 4. For the Hα emission, galaxies, background sources, and H II regions are all excluded. The same *Subaru* three-colour composite image as shown in Fig. 2 is shown here, with the X-ray contours in green. Right-hand panel: the measured Hα and X-ray surface brightnesses for these five regions in red are plotted with the best-fitting linear relation and all data points in black from Sun et al. (2021). For the A1367 OC, while the correlation around the Hα cloud is consistent with those for stripped tails still attached to their parent galaxies, the X-ray-to-Hα ratios are typically higher, which should not be a surprise for the OC in a much more advanced stage of evolution than the stripped tails. Note that only generous upper limits on the total Hα emission are put for regions 4 and 5.

4 DISCUSSION

4.1 Origin of the OC

First, we check if the X-ray OC is a background galaxy cluster. We examined the X-ray spectral properties of the OC assuming different z, exceeding 0.024. For each assumed z, the best-fitting T_X and L_X are

derived. If the OC is a background cluster, it should lie on the L_X-T_X relation for groups and clusters (e.g. Giles et al. 2016). This analysis constrains the redshift to the range $0.14 < z < 0.29$ for the X-ray OC (1 arcmin = 148–261 kpc at this z range). L_* galaxies in clusters in this redshift range should have an r-band magnitude of 17.8–19.6 AB mag, well within the detection limit of *SDSS*. However, within 150 kpc of the X-ray peak (for $z = 0.14 - 0.29$), none of the *SDSS*

sources with a 'type' of GALAXY is brighter than the above *r*-band magnitude. This is also shown from our deep *Subaru* data at the *B*, *R* (including HSC's *r*-band) and *i*-bands. Since the brightest central galaxy (BCG) is typically more than five times more luminous than L_*, we can rule out the scenario that the X-ray OC is a background cluster.

Then the origin of the OC may be an infalling galaxy group or the stripped ISM from a massive galaxy. For the temperature of the OC (1.6 keV), the expected X-ray luminosity is $L_{bol} = 7.1 \times 10^{42}$ erg s^{-1} from the $L_X - T_X$ relation of galaxy clusters and groups (e.g. Giles et al. 2016), which is over 20 times higher than the observed value. Can the OC be the remnant of an infalling galaxy group? A galaxy group this massive almost always has a BCG more luminous than L_*. However, we examined the *2MASS* Extended Source Catalog and found no E/S0 galaxies of brighter than $0.8 L_*$ (Kochanek et al. 2001) within $0.5 r_{500, infallgroup} \approx 300$ kpc of the OC (from $r_{500} - T_X$ relation; Sun et al. 2009). Moreover, the remnant X-ray core of an infalling galaxy group typically does not have associated Hα emission. Thus, it is unlikely the OC is a remnant core of an infalling galaxy group. It's more likely that the OC originates from the stripped ISM of an infalling galaxy. The parent galaxy should not be small, giving the significance of the X-ray gas mass of the OC ($\sim 10^{10}$ M$_\odot$). It may not be accidental to find the OC in the NW of A1367, because A1367 is located in a node of the cosmic web. Several galaxy groups with a higher fraction of SF galaxies are falling into it, especially in the NW direction, and the stripping processes may be very active there (Cortese et al. 2004). Galaxies with stripped HI gas (Scott et al. 2018) and Hα tails (Yagi et al. 2017) preferentially gather around in the same region of the cluster.

Isolated Hα clouds like the OC are rare in galaxy clusters, e.g. none found in the Hα surveys in the Coma cluster, A851, and CL0024+17 (Yagi et al. 2010, 2015). The only other isolated Hα cloud in a galaxy cluster we are aware of is SECCO 1 in the Virgo cluster (Beccari et al. 2017; Sand et al. 2017; Bellazzini et al. 2018). SECCO 1 is a faint, star-forming stellar system with some diffuse Hα emission. Its physical size, ~ 1.2 kpc in radius for each of the two pieces (Bellazzini et al. 2018), is much smaller than the OC discussed in this paper. It has a rather high metallicity of $\sim$half solar for its low optical luminosity (Beccari et al. 2017; Sand et al. 2017). Beccari et al. (2017) suggested that SECCO 1 was formed from a pre-enriched gas cloud, possibly stripped from a massive galaxy in the Virgo cluster. There is no report of an X-ray counterpart of SECCO 1 and the properties of SECCO 1 appear very different from those of the A1367 OC. Future wide-field Hα surveys (e.g. VESTIGE, Boselli et al. 2018) should be able to constrain the abundance of isolated Hα clouds in clusters.

4.2 Pressure balance in the X-ray OC

A1367 is undergoing a merger along the NW-SE direction (e.g. Sun & Murray 2002; Ge et al. 2019b). We can approximate its X-ray surface brightness distribution with two superimposed β-models of $I = I_{01}(1 + r_1^2/r_{c1}^2)^{1/2 - 3\beta_1} + I_{02}(1 + r_2^2/r_{c2}^2)^{1/2 - 3\beta_2}$, each centred on a subcluster as shown in Fig. 9. Before we fit the SBP of the SE subcluster with a β-model, we mask out the NW subcluster beyond the dashed line (0–120 deg counterclockwise from the west) in Fig. 9. Then the image of the NW subcluster is obtained by subtracting the first β-model from the original diffuse cluster image as shown in Fig. 9 middle panel. We fit the second β-model to the NW subcluster. The Fig. 9 right-hand panel shows the residual emission after subtraction these two β-models from the original image. While the residual large-scale features may be sensitive to

the model properties (e.g. centroid, asymmetry), the small residual features are robust. The residual image of Fig. 9 right-hand panel reveals some significant features, including a cold front in the SE subcluster (Ghizzardi, Rossetti & Molendi 2010), a long X-ray tail of UGC 6697 (Sun et al. 2021), long X-ray trails associated with the Blue Infalling Group (Yagi et al. 2017; Fossati et al. 2019), and the X-ray emission of the OC.

We then derive the ICM density distribution from the best-fitting β-model to the cluster SBPs. We note that this method assumes the X-ray surface brightness is proportional to the emission measure as $EM_{model} = \int (n_{e1}^2 + n_{e2}^2) dl$, where $n_{e1} = n_{01}(1 + r_1^2/r_{c1}^2)^{-3\beta_1/2}$ and $n_{e2} = n_{02}(1 + r_2^2/r_{c2}^2)^{-3\beta_2/2}$ are the electron densities of SE and NW subclusters, while the true X-ray surface brightness, assuming two subclusters are merging on the plane of the sky, is proportional to $EM_{true} = \int (n_{e1} + n_{e2})^2 dl$. There is a discrepancy between EM_{model} and EM_{true}, especially between the two peaks of subclusters. However, at the far sides from each peak, the SBP is dominated by the gas density of each subcluster. We can correct the density normalization through comparing the SBP from X-ray observations and the mock SBP from the integral of EM_{true}. After several iterations, the best-fitting parameters of the β-models are $n_{01} = (1.5 \pm 0.1) \times 10^{-3}$ cm^{-3}, $r_{c1} = 209.8 \pm 3.6$ kpc, $\beta_1 = 0.62 \pm 0.01$ for the SE subcluster centred on RA=11^{h}44^{m}50^s.1, Dec.=+19°42$'$14$''$.7; and $n_{02} = (7.1 \pm 0.2) \times 10^{-4}$ cm^{-3}, $r_{c2} = 218.3 \pm 8.4$ kpc, $\beta_2 = 0.57 \pm 0.02$ for the NW subcluster centred on RA=11^{h}44^{m}06^s.3, Dec.=+19°54$'$58$''$.9. The total density is $n_{e, ICM} = 2.9 \times 10^{-4}$ cm^{-3} for cluster gas around the OC (800 kpc from the SE subcluster centre and 450 kpc from the NW subcluster centre). The average temperature is $kT_{ICM} = 2.9 \pm 0.2$ keV for the ICM in an annulus of 60–100 kpc around the OC. Then the ICM thermal pressure is $P_{ICM} = kn_{tot}T_{ICM} = kn_{e, ICM} \cdot n_{tot}/n_e \cdot T_{ICM} = 2.6 \times 10^{-12}$ dyn cm^{-2}, while the ram pressure from ICM is $P_{ram} = \rho_{ICM} v_{OC}^2 = 5.6 \times 10^{-12} (v_{OC}/1000$ km s$^{-1})^2$ dyn cm^{-2}. This can be compared with the thermal pressure inside the OC, $P_{OC} = 1.5 \times 10^{-11}$ dyn cm^{-2}, from the average density. Thus, the X-ray OC would be over-pressurized on sides not experiencing ram pressure, assuming a single T for the OC. Including a density gradient in the OC can alleviate the pressure imbalance at the edge but the OC is still over-pressurized. Without an associated dark matter halo, the OC has to expand.

We can also examine the pressure balance assuming two phases of gas, with the 2 APEC fitting result in Table 2 (the one with the same abundance for both phases). The pressure ratio for two phases is $\frac{P_1}{P_2} = \frac{n_1 T_1}{n_2 T_2} = 1$. The normalization ratio of two APEC model is $\frac{N_1}{N_2} = \frac{n_1^2 f_1}{n_2^2 f_2}$, where f_1 and f_2 are volume occupation factor for cool and hot phase gas and $f_1 + f_2 = f$. Combining previous equations, we get

$$f_1 = f \frac{N_1}{N_2} \bigg/ \left[\left(\frac{T_2}{T_1}\right)^2 + \frac{N_1}{N_2} \right]. \qquad (2)$$

The resultant $f_1 = 0.03f$ and $f_2 = 0.97f$, thus the hotter phase gas occupies 97 per cent of the volume of the soft X-ray emitting gas. The electron density of cool and hot phase is $n_{e, cool} = 8.5 \times 10^{-3} f^{-1/2}$ cm^{-3} and $n_{e, hot} = 2.3 \times 10^{-3} f^{-1/2}$ cm^{-3}, respectively. The total gas mass is $M_{OC, 2T} = 1.2 \times 10^{10} f^{1/2}$ M$_\odot$. The ISM thermal pressure is $P_{OC, 2T} = 2.6 \times 10^{-11}$ dyn cm^{-2}. Thus, the pressure imbalance is even worse with the two-T model. There is a similar issue of pressure imbalance for stripped X-ray tails still attached to a galaxy (e.g. Sun et al. 2010; Zhang et al. 2013). It is unclear whether pressure balance exists at the OC/ICM interface but possible solutions for the pressure imbalance include modelling uncertainty of the X-ray spectra (especially related to abundance), extra pressure
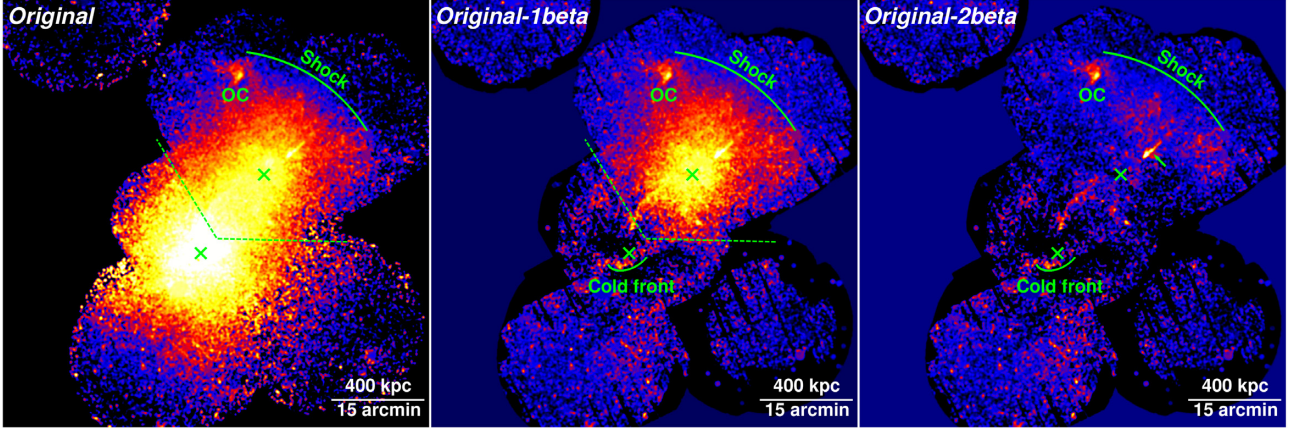
Figure 9. Original and residual X-ray images of A1367. Left-hand panel: the 0.7–1.3 keV *XMM* mosaic of A1367, with background subtracted and exposure corrected. X-ray point sources are also removed in this mosaic to show the diffuse emission better. The dashed line marks the boundary between the SE and NW subclusters, for the purpose of double β-model fit to the SBP of the cluster. Two green crosses mark the centres of two β-models for the SBP fitting. The positions of the OC and the shock front are also marked. Middle panel: residual emission after subtracting the first β-model centred on the SE subcluster. Regions (e.g. CCD edges and gaps) with low exposure time and limited statistics have been removed. The NW subcluster and a cold front to the south of the SE subcluster core are significant. Right-hand panel: residual emission after further subtracting the second β-model centred on the NW subcluster. The long X-ray tail of UGC 6697 is marked by a green arrow. The OC also appears as a significant residual feature.

support in the ICM from magnetic field and turbulence, and the contribution of charge exchange to the X-ray emission in stripped gas (e.g. Zhang et al. 2013).

4.3 ICM microphysics of the OC

The OC has been detached from the parent galaxy and the dark matter halo, it also presents an ideal example to study the ICM microphysics. How does it survive disruption by the Rayleigh–Taylor (RT) and Kelvin–Helmholtz (KH) instabilities, as well as the thermal conduction?

The KH instability occurs when there is a velocity difference across the interface between two fluids. The typical mass loss rate due to KH instability is (Nulsen 1982)

$$\dot{M}_{\rm KH} \approx \pi R_{\rm OC}^2 \rho_{\rm ICM} v_{\rm OC} = 23.9 \left(\frac{n_{\rm e,ICM}}{2.9 \times 10^{-4}\ {\rm cm}^{-3}} \right) \left(\frac{R_{\rm OC}}{30\ {\rm kpc}} \right)^2$$
$$\times \left(\frac{v_{\rm OC}}{1000\ {\rm km\ s}^{-1}} \right) {\rm M}_\odot\ {\rm yr}^{-1}. \qquad (3)$$

The mass loss time-scale for the OC is $t_{\rm KH} = M_{\rm OC}/\dot{M}_{\rm KH} = 4.2 \times 10^8$ yr. The KH instability can be suppressed by magnetic field if $\frac{B^2(\rho_1+\rho_2)}{2\pi\rho_1\rho_2(v_1-v_2)^2} \geq 1$ (Chandrasekhar 1961), where B is the average tangential magnetic field of two fluids beside the interface. In this case, $v_1 - v_2 = v_{\rm OC}$, $\rho_1 = \rho_{\rm OC}$, $\rho_2 = \rho_{\rm ICM}$, and $\rho_{\rm OC} \gg \rho_{\rm ICM}$, we assume $B = 6\ \mu G$, thus the condition for suppression of KH instability is

$$\frac{B^2}{2\pi\rho_{\rm ICM} v_{\rm OC}^2} = 1.02 \left(\frac{B}{6\ \mu G} \right)^2 \left(\frac{n_{\rm e,ICM}}{2.9 \times 10^{-4}\ {\rm cm}^{-3}} \right)^{-1}$$
$$\times \left(\frac{v_{\rm OC}}{1000\ {\rm km\ s}^{-1}} \right)^{-2} \geq 1. \qquad (4)$$

The typical magnetic field is a few μG (e.g. Carilli & Taylor 2002; Bonafede et al. 2010) in the ICM. However, magnetic fields can be amplified by cluster merge shocks (e.g. Donnert et al. 2018), and OC is likely in the post-shock region. Moreover, the magnetic field near a moving cloud can be significantly strengthened by the formation

of a parallel magnetic field layer via magnetic draping (e.g. Dursi & Pfrommer 2008; Müller et al. 2021). Thus, a magnetic field with a strength of $\sim6\ \mu G$ around the OC is possible and could suppress the KH instability.

The RT instability occurs in an interface between two fluids of different densities, when the lighter fluid is pushing the heavier one typically due to a gravitational field or an acceleration. An equivalent situation applied here is the dense OC cloud moving through the rarefied ICM. The drag force on the OC cloud is $F_{\rm d} = C_{\rm d}\rho_{\rm ICM} v_{\rm OC}^2 A/2$, where $C_{\rm d} \approx 0.5$ is the drag coefficient assuming a sphere shape for OC, $A = \pi R_{\rm OC}^2$ is the cloud cross-sectional area, and $\rho_{\rm ICM} v_{\rm OC}^2$ is the ram pressure $P_{\rm ram}$ from ICM. The relevant acceleration is $a = F_{\rm d}/M_{\rm OC} = \frac{3C_{\rm d} P_{\rm ram}}{8\rho_{\rm OC} R_{\rm OC}} = 1.9 \times 10^{-9}\ {\rm cm\ s}^{-2}$, where $\rho_{\rm OC}$ is the OC density from the hot gas as the OC may not have an associated dark matter halo. The RT instability would tear the cloud apart in a few characteristic e-folding times

$$t_{\rm RT} = \left(\frac{\lambda}{2\pi a} \right)^{1/2} = 8.8 \times 10^7 \left(\frac{\lambda}{30\ {\rm kpc}} \right)^{1/2}$$
$$\times \left(\frac{a}{1.9 \times 10^{-9}\ {\rm cm\ s}^{-2}} \right)^{-1/2}\ {\rm yr}, \qquad (5)$$

where λ is the scale-length of the RT perturbation. The RT instability can be stabilized by mechanisms such as self-gravity and magnetic fields (Chandrasekhar 1961). The self-gravitational acceleration of OC $g_{\rm OC} = \frac{GM_{\rm OC}}{R_{\rm OC}^2} = 1.6 \times 10^{-10}\ {\rm cm\ s}^{-2}$, which is much smaller than a; thus the gas self-gravity is insufficient to suppress the RT instability. The tension of magnetic field can suppress the growth of perturbations of scale-length $\lambda < \lambda_c$ with

$$\lambda_c = \frac{B^2 \cos^2\theta}{a(\rho_{\rm OC} - \rho_{\rm ICM})} = 511 \left(\frac{B}{6\ \mu G} \right)^2 \left(\frac{a}{1.9 \times 10^{-9}\ {\rm cm\ s}^{-2}} \right)^{-1}$$
$$\times \left(\frac{n_{\rm e,OC}}{3.1 \times 10^{-3}\ {\rm cm}^{-3}} \right)^{-1}\ {\rm kpc}, \qquad (6)$$

where an average value of $\langle \cos^2\theta \rangle = 1/2$ is used and $\rho_{\rm OC} \gg \rho_{\rm ICM}$ thus $\rho_{\rm ICM}$ is ignored here. The λ_c is 17 times larger than the radius of

the OC cloud, thus a magnetic field around 6 μG can also suppress the RT instability effectively.

The thermal conduction can smear out the temperature gradient between the OC and nearby ICM, i.e. the cooler OC evaporates in the hotter ICM. We can compare the size of the OC with a critical length called 'Field length' (e.g. McKee & Begelman 1990):

$$\lambda_F = \left(\frac{\kappa T}{n^2 \Lambda}\right)^{1/2} = 2.2 \left(\frac{T_{ICM}}{2.9\,keV}\right)^{7/4} \left(\frac{n_{e,ICM}}{2.9 \times 10^{-4}\,cm^{-3}}\right)^{-1}$$

$$\times \left(\frac{\Lambda}{10^{-22.5}\,erg\,s^{-1}cm^3}\right)^{-1/2} Mpc, \quad (7)$$

where $\kappa = 5.6 \times 10^{-7} T^{5/2}$ erg s^{-1} K^{-1} cm^{-1} is the Spitzer conductivity (Spitzer 1962) and Λ is the X-ray cooling rate (e.g. Schure et al. 2009). The OC size is much smaller than the λ_F, thus it will be evaporated by thermal conduction from the hot surrounding ICM on a conduction time-scale (e.g. Sarazin 1988) of:

$$t_{cond} = \frac{nkl^2}{\kappa} = 2.9 \times 10^7 \left(\frac{n_{e,ICM}}{2.9 \times 10^{-4}\,cm^{-3}}\right)$$

$$\times \left(\frac{R_{OC}}{30\,kpc}\right)^2 \left(\frac{T_{ICM}}{2.9\,keV}\right)^{-5/2} yr. \quad (8)$$

The OC can only travel for a distance of $d = v_{OC} \times t_{cond} \sim 30(v_{OC}/1000\,km\,s^{-1})$ kpc, which is too short. The thermal conduction has to be suppressed significantly. Previous studies suggest that magnetic field can help to suppress the thermal conduction by two orders of magnitude relative to the classical Spitzer value, which is beneficial to the survival of OC in the ICM (e.g. Carilli & Taylor 2002; Markevitch & Vikhlinin 2007).

4.4 Excitation mechanism of the warm, ionized gas in OC

The line diagnostics show LI(N)ER-like emission for the OC. Several excitation mechanisms may produce LI(N)ER-like emission, such as photoionization by AGN and hot evolved stars, radiative shocks, photoionization and thermal conduction from the hot (T $\gg 10^4$ K) ICM (Ho 2008; Yan & Blanton 2012; Kewley, Nicholls & Sutherland 2019 and references therein). In the outer stripped tails of ESO 137-001, emission-line flux ratios similar to those in A1367 OC have been found and explained as the results of photoionization (stripped ionized gas or *in situ* H II regions) plus radiative shocks (Fossati et al. 2016). For A1367 OC, the slow radiative shock models (Rich et al. 2011) are not able to reproduce the observed [O I]/H α flux ratios. In addition, the median velocity dispersion of the ionized gas is only $\sim$80 km s^{-1}, which is too low for shocks.

The OC has very weak SF at most. The *GALEX* data in this field, with 3953 s of exposure at the Far-Ultraviolet (FUV) and 4340 s of exposure at the Near-Ultraviolet (NUV), are much deeper than the *XMM* OM UVM2 data. The lack of any *GALEX* source in the *MUSE* field of the OC gives an upper limit on the SFR at 6×10^{-4} M$_\odot$ yr^{-1}, with the calibration from Kennicutt & Evans (2012). We also attempted to select H II region candidates from the *MUSE* H α surface brightness map with SEXTRACTOR. By requesting point-like sources (CLASS_STAR > 0.9) with a low ellipticity (*e* < 0.2), only one candidate at RA = 11^{h}44^{m}21^s.4 and Dec. = +20°10$'$14$''$.6 is identified. This candidate is also shown as the most compact clump in the *Subaru* net H α image. However, as shown in Fig. 3, it is off the main cloud and rather isolated. As this source is too faint, we cannot unambiguously confirm it as an H II region from its *MUSE* spectrum. The H α luminosity of this source is 2.8×10^{37} erg s^{-1} (without intrinsic extinction), which would correspond to a

SFR of 1.5×10^{-4} M$_\odot$ yr^{-1}, with the calibration from Kennicutt & Evans (2012). The lack of even weak SF in the OC excludes young stars as the main ionization source. However, there is SF ongoing in the whole cloud complex beyond the *MUSE* field, as shown in Yagi et al. (2017) and the two likely H II regions observed with *APO/DIS*.

The models of photoionization from the hot ICM (Voit & Donahue 1990; Donahue & Voit 1991) also have difficulty accounting for the observed emission-line flux ratios, especially the [O III]/H β flux ratios. Campitiello et al. (2021) particularly used $kT \sim 1$ keV plasma as the ionizing source in an RPS galaxy from GASP, but with the similar issues as before, also because the ionization parameter needs to be sufficiently large enough to account for the bulk of the observed optical line emission (or the line ratios are not the only constraints). Ferland et al. (2009) proposed collisional ionization (by cosmic rays and dissipation of magnetohydrodynamic wave energy) to explain the filament emission in galaxy clusters. While the predicted [N II]/H α, [S II]/H α, and [O I]/H α are close to our observational results, the [O III]/H β flux ratios are still under-predicted by at least two orders of magnitude. Further development of models and multiwavelength diagnostics (i.e. infrared and ultraviolet lines) may help to explore the excitation mechanism of the LI(N)ER-like emission in A1367 OC.

While the metallicity of the warm, ionized gas would provide important information on its parent, the unclear ionization mechanism prevents a robust estimate of the metallicity. If we simply adopt the diagnostics for H II regions, the derived metallicity is log(O/H) + 12 = 8.5−8.9 from the [N II]λ6584 / [S II]$\lambda\lambda$ 6716, 6731 and the [N II]λ6584 / H α ratios, with the diagnostics derived by Kewley & Dopita (2002). This about solar metallicity would imply a massive parent for the OC. For the only H II region candidate, the same diagnostics result in a metallicity of 8.6–8.8, consistent with the above estimate.

4.5 A signpost of ICM clumping and turbulence

After being stripped far away from the parent galaxy, now the OC is a clump in the ICM of A1367. The clumpiness of the ICM has been studied with X-ray observations from the surface brightness fluctuations (e.g. Churazov et al. 2012; Morandi et al. 2017) or ICM radial profiles (e.g. Simionescu et al. 2011; Walker et al. 2013; Eckert et al. 2015), especially at the cluster outskirt, because the gas clumping factor increases with the cluster radius suggested by simulations (e.g. Nagai & Lau 2011; Vazza et al. 2013). For example, Vazza et al. (2013) found that the typical X-ray clump size is <69 kpc and the typical bolometric luminosity is $L_{bol} = 4 \times 10^{39}−1.5 \times 10^{42}$ ergs s^{-1}. The overall properties of the OC are consistent with the predicted properties of large/luminous ICM clumps from simulations. As a signpost of the ICM clumping in the nearby cluster A1367, we have a rare opportunity to study an ICM clump in detail.

Apart from providing additional non-thermal pressure to balance gravity, the ICM turbulence can also re-accelerate relativistic electrons and amplify the magnetic field to produce radio halo emission (e.g. Fujita, Takizawa & Sarazin 2003; Brunetti & Lazarian 2007; Beresnyak & Miniati 2016; Donnert et al. 2018); distribute energy and metals from AGN and stellar feedback (e.g. Rebusco et al. 2006; Gaspari, Ruszkowski & Sharma 2012; Zhuravleva et al. 2014); dissolve the ISM of galaxies through turbulent viscous stripping (e.g. Roediger & Hensler 2005). The turbulence is generated from cluster merger or accretion of matter, cool core sloshing, and jet outflows from AGN (e.g. Vazza, Roediger & Brüggen 2012). The

measurements of turbulence in cluster central regions directly from line width (e.g. Sanders et al. 2010; Hitomi Collaboration 2016) or indirectly from density/pressure fluctuation (e.g. Schuecker et al. 2004; Churazov et al. 2012) suggest that the ratio of turbulent pressure to thermal pressure in the ICM is small, i.e. ≲10 per cent. As for the clumping factor, simulations (e.g. Lau et al. 2009) also suggest that the turbulence increases with cluster radius. Although the indirect measurements (e.g. Khatri & Gaspari 2016; Eckert et al. 2019) support this trend, there is limited observational evidence from direct measurements.

The multi-phase nature of OC provides us an opportunity to study the ICM turbulence at the cluster outskirt. As warm gas mixing with hot gas, the kinematics of multiphase gas are tightly linked, such a connection has been proposed in cool cores (Gaspari et al. 2018). The velocity dispersion of the warm gas is rather low, $\sim$80 km s^{-1} (Fig. 3), which is much smaller than the sound speed in the hot gas (650–870 km s^{-1} for $kT = 1.6-3.0$ keV). The ratio of turbulent pressure to the ICM thermal pressure in the OC is only $\sim$1 per cent, if the kinematics of the warm ionized gas trace the kinematics of the ICM in this case. Moreover, such a level of turbulence may be able to induce the slow top-down turbulent condensation from the ICM as suggested by the condensation criterion C-ratio $C \equiv t_{cool}/t_{eddy}$, where $t_{eddy} = 2\pi r^{2/3} L^{1/3}/\sigma_{v,L}$ is the turbulence eddy turnover time (Gaspari et al. 2018). In the case of the OC, we use a radius $r = 30$ kpc, or a full size of cloud $L = 60$ kpc, and a mean 3D velocity dispersion $\sigma_{v,L} = \sqrt{3}\sigma_{v,1d} = 139$ km s^{-1}. We then have $t_{cool} = 3.6-7.2$ Gyr and $t_{eddy} = 1.6$ Gyr that returns a $C = 2.3-4.5$, which indicates the condensation may be significant over the long term. Therefore, the OC may grow via slow ICM condensation and accretion, akin to an off-centre chaotic cold accretion rain (Gaspari, Temi & Brighenti 2017). Such kind of growth for intracluster clouds is also suggested in the simulation (e.g. Sparre, Pfrommer & Ehlert 2020; Kanjilal, Dutta & Sharma 2021).

5 CONCLUSION

We have discovered an OC detected in both Hα and X-rays in the outskirt of the merging galaxy cluster A1367, with a projected distance of $\sim$800 kpc to the cluster centre. Our main conclusions are as follows:

(1) The cloud most likely originates from the stripped ISM of an infalling galaxy. The parent galaxy is still unknown and maybe a massive one, because the OC has an X-ray bolometric luminosity of $\sim$3.1 × 10^{41} erg s^{-1} and a hot gas mass of $\sim$10^{10} M$_\odot$. The metallicity of the Hα OC also suggests a massive parent galaxy.

(2) By being stripped and far away from the parent galaxy, now the OC is a signpost of the ICM clumping. It may be in an advanced evolutionary stage suggested by a higher average X-ray temperature of 1.6 keV than typical X-ray tails and generally high X-ray-to-Hα ratios than stripped tails still attached to their parent galaxies.

(3) The Hα peak of the OC has an offset of $\sim$12 kpc from the X-ray peak of the OC, with several Hα filaments enclosing the X-ray peak. The bright Hα clumps may be associated with the only surviving cold clouds mixing with the ICM.

(4) The Hα OC shows a velocity gradient along the east-west direction as an indication of cloud's motion, but with a low level of velocity dispersion ($\sim$80 km s^{-1}) likely indicating a low level of the ICM turbulence.

(5) The line diagnostics from *MUSE* suggest little SF in the main Hα OC and a LI(N)ER-like spectrum. The non-detection of *GALEX* source in the *MUSE* field of the OC gives an upper limit on the SFR

at $\sim$10^{-3} M$_\odot$ yr^{-1} for the main body of the Hα OC, but some SF is present to the SE of OC.

(6) It is found that a magnetic field around 6 μG can suppress hydrodynamic instabilities (RT and KH instabilities) and thermal conduction to help the survival of the cloud in the harsh ICM environment.

This discovery of an isolated X-ray clump accompanied by Hα emission suggests that some ICM clumps are multiphase. Future multiwavelength observations can explore the multiphase nature of ICM clumps better, and link them to the related multiphase processes of cool cores (e.g. Gaspari, Tombesi & Cappi 2020). Moreover, this discovery suggests that we can potentially probe ICM clumping with future sensitive and wide-field Hα surveys (e.g. Boselli et al. 2018). The kinematics of the ICM may also be explored with warm gas in the future.

While the OC is only the first ICM clump detected in both X-rays and Hα, and ICM clumps as luminous as the OC may be rare, the number of similar examples should grow with more sensitive X-ray (e.g. *eROSITA*) and Hα data to survey nearby galaxy clusters. ICM clumps as luminous as the A1367 OC can be detected with 30 ks clean *XMM* time up to $z = 0.056$. Similarly, with 80 ks clean *Chandra* ACIS-I time, we can detect the same clump out to $z = 0.050$ ($z = 0.039$) with the *Chandra* cycle 5 (cycle 23) response. The detection does depend on the local ICM background. If the local ICM background is increased by a factor of 3, 30 ks clean *XMM* observation can only detect the OC up to $z = 0.048$. Hα clouds like the A1367 OC can also be detected to the above z with the similar Hα narrow-band imaging data as those in Yagi et al. (2017). The multiwavelength surveys and studies will be necessary for us to better understand the multiphase isolated clouds in clusters.

DATA AVAILABILITY

The *XMM-Newton* raw data used in this paper are available to download at the HEASARC Data Archive website.[1] The *MUSE* raw

---

[1] https://heasarc.gsfc.nasa.gov/docs/archive.html

data are available to download at the ESO Science Archive Facility.[2] The reduced data underlying this paper will be shared on reasonable requests to the corresponding authors.

REFERENCES

Asplund M., Grevesse N., Sauval A. J., Scott P., 2009, ARA&A, 47, 481
Bacon R. et al., 2010, in McLean I. S., Ramsay S. K., Takami H., eds, Proc. SPIE Conf. Ser. Vol. 7735, Ground-based and Airborne Instrumentation for Astronomy III. SPIE, Bellingham, p. 773508
Bacon R., Piqueras L., Conseil S., Richard J., Shepherd M., 2016, Astrophysics Source Code Library, record ascl:1611.003
Beccari G. et al., 2017, MNRAS, 465, 2189
Bellazzini M. et al., 2018, MNRAS, 476, 4565
Beresnyak A., Miniati F., 2016, ApJ, 817, 127
Bertin E., Mellier Y., Radovich M., Missonnier G., Didelon P., Morin B., 2002, in Bohlender D. A., Durand D., Handley T. H., eds, ASP Conf. Ser. Vol. 281, Astronomical Data Analysis Software and Systems XI. Astron. Soc. Pac., San Francisco, p. 228
Bonafede A., Feretti L., Murgia M., Govoni F., Giovannini G., Dallacasa D., Dolag K., Taylor G. B., 2010, A&A, 513, A30
Bosch J. et al., 2018, PASJ, 70, S5
Boselli A. et al., 2016, A&A, 587, A68
Boselli A. et al., 2018, A&A, 614, A56
Boselli A. et al., 2021, A&A, 646, A139
Boselli A., Gavazzi G., 2006, PASP, 118, 517
Brunetti G., Lazarian A., 2007, MNRAS, 378, 245
Burkhart B., Loeb A., 2016, ApJ, 824, L7
Calura F., Bellazzini M., D'Ercole A., 2020, MNRAS, 499, 5873
Campitiello M. G. et al., 2021, ApJ, 911, 144
Cannon J. M. et al., 2015, AJ, 149, 72
Carilli C. L., Taylor G. B., 2002, ARA&A, 40, 319
Cavaliere A., Fusco-Femiano R., 1976, A&A, 500, 95
Chandrasekhar S., 1961, Hydrodynamic and Hydromagnetic Stability. International Series of Monographs on Physics, Oxford: Clarendon
Chen H. et al., 2020, MNRAS, 496, 4654
Chung A., van Gorkom J. H., Kenney J. D. P., Vollmer B., 2007, ApJ, 659, L115
Churazov E. et al., 2012, MNRAS, 421, 1123
Cid Fernandes R., Stasińska G., Schlickmann M. S., Mateus A., Vale Asari N., Schoenell W., Sodré L., 2010, MNRAS, 403, 1036
Consolandi G., Gavazzi G., Fossati M., Fumagalli M., Boselli A., Yagi M., Yoshida M., 2017, A&A, 606, A83
Cortese L., Gavazzi G., Boselli A., Iglesias-Paramo J., Carrasco L., 2004, A&A, 425, 429
Davies J. et al., 2004, MNRAS, 349, 922
Dolag K., Borgani S., Murante G., Springel V., 2009, MNRAS, 399, 497
Donahue M., Voit G. M., 1991, ApJ, 381, 361
Donnert J., Vazza F., Brüggen M., ZuHone J., 2018, Space Sci. Rev., 214, 122
Duc P.-A., Bournaud F., 2008, ApJ, 673, 787
Dursi L. J., Pfrommer C., 2008, ApJ, 677, 993
Eckert D. et al., 2019, A&A, 621, A40
Eckert D., Roncarelli M., Ettori S., Molendi S., Vazza F., Gastaldello F., Rossetti M., 2015, MNRAS, 447, 2198
ESO CPL Development Team, 2015, Astrophysics Source Code Library, record ascl:1504.003
Ferland G. J., Fabian A. C., Hatch N. A., Johnstone R. M., Porter R. L., van Hoof P. A. M., Williams R. J. R., 2009, MNRAS, 392, 1475
Fitzpatrick E. L., 1999, PASP, 111, 63
Fossati M., Fumagalli M., Boselli A., Gavazzi G., Sun M., Wilman D. J., 2016, MNRAS, 455, 2028
Fossati M., Fumagalli M., Gavazzi G., Consolandi G., Boselli A., Yagi M., Sun M., Wilman D. J., 2019, MNRAS, 484, 2212

Fujita Y., Takizawa M., Sarazin C. L., 2003, ApJ, 584, 190
Gaspari M. et al., 2018, ApJ, 854, 167
Gaspari M., Ruszkowski M., Sharma P., 2012, ApJ, 746, 94
Gaspari M., Temi P., Brighenti F., 2017, MNRAS, 466, 677
Gaspari M., Tombesi F., Cappi M., 2020, Nat. Astron., 4, 10
Gavazzi G., Boselli A., Mayer L., Iglesias-Paramo J., Vílchez J. M., Carrasco L., 2001, ApJ, 563, L23
Gavazzi G., Consolandi G., Yagi M., Yoshida M., 2017, A&A, 606, A131
Ge C. et al., 2019b, MNRAS, 486, L36
Ge C., Wang Q. D., Tripp T. M., Li Z., Gu Q., Ji L., 2016, MNRAS, 459, 366
Ge C., Sun M., Rozo E., Sehgal N., Vikhlinin A., Forman W., Jones C., Nagai D., 2019a, MNRAS, 484, 1946
Ghizzardi S., Rossetti M., Molendi S., 2010, A&A, 516, A32
Giles P. A. et al., 2016, A&A, 592, A3
Gunn J. E., Gott J. Richard I., 1972, ApJ, 176, 1
Hitomi Collaboration, 2016, Nature, 535, 117
Ho L. C., 2008, ARA&A, 46, 475
Jáchym P., Combes F., Cortese L., Sun M., Kenney J. D. P., 2014, ApJ, 792, 11
Kanjilal V., Dutta A., Sharma P., 2021, MNRAS, 501, 1143
Kauffmann G. et al., 2003, MNRAS, 346, 1055
Kenney J. D. P., Tal T., Crowl H. H., Feldmeier J., Jacoby G. H., 2008, ApJ, 687, L69
Kennicutt R. C., Evans N. J., 2012, ARA&A, 50, 531
Kent B. R. et al., 2007, ApJ, 665, L15
Kewley L. J., Dopita M. A., 2002, ApJS, 142, 35
Kewley L. J., Dopita M. A., Sutherland R. S., Heisler C. A., Trevena J., 2001, ApJ, 556, 121
Kewley L. J., Nicholls D. C., Sutherland R. S., 2019, ARA&A, 57, 511
Khatri R., Gaspari M., 2016, MNRAS, 463, 655
Kochanek C. S. et al., 2001, ApJ, 560, 566
Lang D., Hogg D. W., Mierle K., Blanton M., Roweis S., 2012, Astrophysics Source Code Library, record ascl:1208.001
Lau E. T., Kravtsov A. V., Nagai D., 2009, ApJ, 705, 1129
Markevitch M., Vikhlinin A., 2007, Phys. Rep., 443, 1
Mateos S. et al., 2008, A&A, 492, 51
McKee C. F., Begelman M. C., 1990, ApJ, 358, 392
Merluzzi P. et al., 2013, MNRAS, 429, 1747
Morandi A., Sun M., Mulchaey J., Nagai D., Bonamente M., 2017, MNRAS, 469, 2423
Müller A. et al., 2021, Nat. Astron., 5, 159
Nagai D., Lau E. T., 2011, ApJ, 731, L10
Nulsen P. E. J., 1982, MNRAS, 198, 1007
Poggianti B. M. et al., 2016, AJ, 151, 78
Quilis V., Moore B., Bower R., 2000, Science, 288, 1617
Rebusco P., Churazov E., Böhringer H., Forman W., 2006, MNRAS, 372, 1840
Rich J. A., Kewley L. J., Dopita M. A., 2011, ApJ, 734, 87
Richards G. T. et al., 2015, ApJS, 219, 39
Roediger E., Hensler G., 2005, A&A, 433, 875
Sand D. J. et al., 2017, ApJ, 843, 134
Sanders J. S., Fabian A. C., Smith R. K., Peterson J. R., 2010, MNRAS, 402, L11
Sarazin C. L., 1988, X-ray Emission from Clusters of Galaxies. Cambridge Univ. Press, Cambridge
Schlafly E. F., Finkbeiner D. P., 2011, ApJ, 737, 103
Schlegel D. J., Finkbeiner D. P., Davis M., 1998, ApJ, 500, 525
Schuecker P., Finoguenov A., Miniati F., Böhringer H., Briel U. G., 2004, A&A, 426, 387
Schure K. M., Kosenko D., Kaastra J. S., Keppens R., Vink J., 2009, A&A, 508, 751
Scott T. C., Brinks E., Cortese L., Boselli A., Bravo-Alfaro H., 2018, MNRAS, 475, 4648
Simionescu A. et al., 2011, Science, 331, 1576
Sivanandam S., Rieke M. J., Rieke G. H., 2010, ApJ, 717, 147
Smith R. J. et al., 2010, MNRAS, 408, 1417
Soto K. T., Lilly S. J., Bacon R., Richard J., Conseil S., 2016, MNRAS, 458, 3210

[2]http://archive.eso.org/cms.html

Sparre M., Pfrommer C., Ehlert K., 2020, MNRAS, 499, 4261

Spitzer L., 1962, Physics of Fully Ionized Gases, 2nd edn. Interscience, New York

Sun M. et al., 2021, preprint (arXiv:2103.09205)

Sun M., Murray S. S., 2002, ApJ, 576, 708

Sun M., Jones C., Forman W., Vikhlinin A., Donahue M., Voit M., 2007a, ApJ, 657, 197

Sun M., Donahue M., Voit G. M., 2007b, ApJ, 671, 190

Sun M., Voit G. M., Donahue M., Jones C., Forman W., Vikhlinin A., 2009, ApJ, 693, 1142

Sun M., Donahue M., Roediger E., Nulsen P. E. J., Voit G. M., Sarazin C., Forman W., Jones C., 2010, ApJ, 708, 946

Taylor R., Davies J. I., Auld R., Minchin R. F., 2012, MNRAS, 423, 787

Taylor R., Davies J. I., Jáchym P., Keenan O., Minchin R. F., Palouš J., Smith R., Wünsch R., 2016, MNRAS, 461, 3001

Vazza F., Roediger E., Brüggen M., 2012, A&A, 544, A103

Vazza F., Eckert D., Simionescu A., Brüggen M., Ettori S., 2013, MNRAS, 429, 799

Voit G. M., Donahue M., 1990, ApJ, 360, L15

Walker S. A., Fabian A. C., Sanders J. S., Simionescu A., Tawara Y., 2013, MNRAS, 432, 554

Weilbacher P. M. et al., 2020, A&A, 641, A28

Weilbacher P. M., Streicher O., Urrutia T., Jarno A., Pécontal-Rousset A., Bacon R., Böhm P., 2012, in Radziwill N. M., Chiozzi G., eds, Proc. SPIE Conf. Ser. Vol. 8451, Software and Cyberinfrastructure for Astronomy II. SPIE, Bellingham, p. 84510B

Willingale R., Starling R. L. C., Beardmore A. P., Tanvir N. R., O'Brien P. T., 2013, MNRAS, 431, 394

Yagi M. et al., 2010, AJ, 140, 1814

Yagi M., Komiyama Y., Yoshida M., Furusawa H., Kashikawa N., Koyama Y., Okamura S., 2007, ApJ, 660, 1209

Yagi M., Gu L., Fujita Y., Nakazawa K., Akahori T., Hattori T., Yoshida M., Makishima K., 2013, ApJ, 778, 91

Yagi M., Gu L., Koyama Y., Nakata F., Kodama T., Hattori T., Yoshida M., 2015, AJ, 149, 36

Yagi M., Yoshida M., Gavazzi G., Komiyama Y., Kashikawa N., Okamura S., 2017, ApJ, 839, 65

Yan R., Blanton M. R., 2012, ApJ, 747, 61

Yoshida M. et al., 2002, ApJ, 567, 118

Yoshida M. et al., 2008, ApJ, 688, 918

Yoshida M., Yagi M., Komiyama Y., Furusawa H., Kashikawa N., Hattori T., Okamura S., 2012, ApJ, 749, 43

Zhang B. et al., 2013, ApJ, 777, 122

Zhuravleva I. et al., 2014, Nature, 515, 85

This paper has been typeset from a TeX/LaTeX file prepared by the author.